Stellar evolution of massive stars
at very low metallicities

R. Hirschi, C. Fröhlich, M. Liebendörfer and F.-K. Thielemann

Dept. of Physics and Astronomy, University of Basel
Klingelbergstr. 82, 4056 Basel, Switzerland
raphael.hirschiunibas.ch

Abstract

Recently, measurements of abundances in extremely metal poor (EMP) stars have brought new constraints on stellar evolution models. Indeed, these stars are believed to have been enriched only by one or a few stars. The abundances observed in EMP stars can therefore be almost directly compared with the yields of very metal poor or metal free stars. This removes the complex filter of chemical evolution models. In an attempt to explain the origin of the abundances observed, we computed pre–supernova evolution models, explosion models and the related nucleosynthesis. In this paper, we start by presenting the pre-SN models of rotating single stars with metallicities ranging from solar metallicity down to almost metal free. We then review key processes in core-collapse and bounce, before we integrate them in a simplistic parameterization for 3D MHD models, which are well underway and allow one to follow the evolution of the magnetic fields during collapse and bounce. Finally, we present explosive nucleosynthesis results including neutrino interactions with matter, which are calculated using the outputs of the explosion models.

The main results of the pre-SN models are the following. First, primary nitrogen is produced in large amount in models with an initial metallicity $Z = 10^{-8}$. This large production is due to mixing of carbon and oxygen in the H-burning shell and the main production occurs between core helium and carbon burnings. Second, at the same metallicity of $Z = 10^{-8}$ and for models with an initial mass larger than about 60 $M_\odot$, rotating models may experience heavy mass loss (up to more than half of the initial mass of the star). Several solar masses are lost during the main sequence when the star reaches break-up velocities. The largest amount of mass is lost during the red supergiant stage after rotational mixing and convection have enriched the surface in CNO elements and therefore increased its metal content. The chemical composition of these winds can qualitatively reproduce the abundance patterns observed at the surface of carbon-rich EMP stars. Third, our models predict an upturn of C/O at very low metallicities. Explosive nucleosynthesis including neutrino-matter interactions produce improved abundances for iron group elements, in particular for scandium and zinc. It also opens the way to a new neutrino and proton rich process (νp-process) able to contribute to the nucleosynthesis of elements with $A > 64$.

1 Introduction

Massive stars ($M \gtrsim 10M_\odot$) play an important role in astrophysics. They are the progenitors of blue supergiants (BSG), red supergiants (RSG), Wolf-Rayet (WR) and luminous blue variable (LBV) stars. At the end of their life, they explode as type II or Ib,c supernovae (SN) and maybe also as long soft gamma-ray bursts (GRB). Their cores after collapse become neutron stars (NS) or black holes (BH). They are one of the main sites for nucleosynthesis, which takes place during both pre-SN (hydrostatic) burnings as well as during explosive burnings. A weak s-process occurs during H-burning and r-process probably occurs during the explosion. Radioactive isotopes like ^{26}Al and ^{60}Fe detected by the INTEGRAL satellite are produced by massive stars. Massive stars even though they are much less numerous than low mass stars contribute significantly to the integrated luminosity of galaxies.

At high redshifts (z, or low metallicities Z), their importance grows. The first stars formed are thought to be all massive or even very massive (Bromm 2005) and to be the cause of the re-ionisation of the universe. Finally, recent surveys of metal poor halo stars provide many constraints for the early chemical evolution of our Galaxy (Beers et al. 1992, Beers 1999, Israelian et al. 2004, Christlieb et al. 2004, Cayrel et al. 2004, Spite et al. 2005).

The measured abundances of many elements present a very small scatter down to very low metallicities ([Fe/H]~ -4.2, see Cayrel et al. 2004). This tends to prove that the interstellar medium (ISM) was already well mixed at an early stage. However, r-process elements show a scatter in their abundances contradicting this trend (Ryan...). There is no significant enrichment by pair-instability supernovae (PISN, see Heger and Woosley 2002, Umeda and Nomoto 2002, 2003 for more details). Production of primary nitrogen in massive stars (that died before the formation of the halo metal poor star) is necessary in order to explain the high abundance of nitrogen observed.

About a quarter of the extremely metal poor (EMP) stars show a strong enrichment of carbon (carbon-rich, CEMP), with [C/Fe]$\sim$2–4, where [A/B] = $\log_{10}(X_A/X_B) - \log_{10}(X_A/X_B)_\odot$. The CEMP stars can probably be divided into two subclasses, the Ba-rich and the Ba-normal stars (see Ryan et al. 2005 and references therein). According to Ryan et al. (2005), the Ba-rich CEMP stars have accreted enriched matter from an AGB stars in a binary system in the course of their life. On the other hand the Ba-normal CEMP stars would have formed from a cloud already enriched in carbon and neutron capture elements. The cloud itself would have been enriched by wind or supernova ejecta from massive stars. The two most metal poor halo stars found up to now, HE0107-5240 ([Fe/H]=-5.3, see Christlieb et al. 2004) and HE1327-2326 ([Fe/H]=-5.5, see Frebel et al. 2005 and Aoki et al 2005) belong to this last group, the Ba-normal CEMP stars. These two stars both present strong but different enrichment in nitrogen and oxygen.

In the light of these recent observational results and following the exploratory work of Meynet et al (2005), we explore the impact that rotation can have in massive very low metallicity stars. In Sect. 2, we present the

pre-SN models, their evolution and stellar yields for different initial masses, rotation velocities and metallicities and compare them with EMP stars. In Sect. 3, we describe the recent update in the explosion models and the corresponding nucleosynthesis in 1D and the latest development of a new 3D MHD model. In Sect. 4 we give our conclusions.

2   Pre-SN models

2.1   Description of the stellar models

The computer model used to calculate the stellar models is described in detail in Hirschi et al (2004). Convective stability is determined by the Schwarzschild criterion. Convection is treated as a diffusive process from oxygen burning onwards. The overshooting parameter is 0.1 H_P for H and He–burning cores and 0 otherwise. Instabilities induced by rotation taken into account are meridional circulation and secular and dynamical shears. The reaction rates are taken from the NACRE (Angulo et al 1999) compilation for the experimental rates and from the NACRE website (http://pntpm.ulb.ac.be/nacre.htm) for the theoretical ones.

At low metallicities the initial chemical composition is calculated in the following way. For a given metallicity Z (in mass fraction), the initial helium mass fraction Y is given by the relation $Y = Y_p + \Delta Y / \Delta Z \cdot Z$, where Y_p is the primordial helium abundance and $\Delta Y / \Delta Z$ the slope of the helium–to–metal enrichment law. $Y_p = 0.24$ and $\Delta Y / \Delta Z = 2.5$ were used according to recent determinations (see Izotov & Thuan 2004 for example). For the mixture of the heavy elements, we adopted the same mixture as the one used to compute the opacity tables for Weiss 95's alpha–enriched composition (Iglesias & Rogers 1996).

The mass loss rates are described and discussed in Meynet, Ekström & Maeder (2005). The mass loss rates (and opacities) are rather well determined for chemical compositions which are similar to solar (or alpha–enriched mixing) composition or similar to a fraction of the solar composition. However, very little was known about the mass loss of very low metallicity stars with a strong enrichment in CNO elements until recently. Vink & de Koter (2005) study the case of WR stars but a crucial case, which has not been studied in detail yet, is the case of red supergiant stars (RSG). As we shall see later, due to rotational and convective mixing, the surface of the star is strongly enriched in CNO elements during the RSG stage. Awaiting for future studies, it is implicitly assumed in this work (as in Meynet, Ekström & Maeder 2005) that CNO elements have a significant contribution to opacities and mass loss rates. Therefore the mass loss rates depend on metallicity as $\dot{M} \sim (Z/Z_\odot)^{0.5}$, where Z is the mass fraction of heavy elements at the surface of the star, also when the iron group elements content is much lower the CNO elements content.

A specific treatment for mass loss was applied at break-up (see Meynet,

Ekström & Maeder 2005). At break-up, the mass loss rate adjusts itself in such a way that an equilibrium is reached between the envelope extension and the removal of gravitationally unbound mass. In practice, however, since the critical limit contains mathematical singularities, we considered that during the break-up phase, the mass loss rates should be such that the model stays near a constant fraction (around 0.95) of the limit.

2.2   Characteristics of the models

The value of 300 km s^{-1} used for the initial rotation velocity at solar metallicity corresponds to an average velocity of about 220 km s^{-1} on the Main Sequence (MS) which is very close to the average observed value (see for instance Fukuda 1982). It is unfortunately not possible to measure the rotational velocity of very low metallicity stars since they all died a long time ago. Nevertheless, there is indirect evidence that stars with a lower metallicity have a higher rotation velocity. Observational evidence is the higher ratio of Be to B stars in the Magellanic clouds compared to our Galaxy (Maeder et al 1999). This can be due to the difficulty of evacuating angular momentum during the star formation, which is even more important at lower metallicities (see Abel et al 2002 for simulations of star formation in the early Universe). Finally, a low metallicity star containing the same angular momentum as a solar metallicity star has a higher surface rotation velocity due to its smaller radius (one quarter of $Z_\odot$ radius for 20 $M_\odot$ stars). It is therefore worth studying models with an initial rotational velocities faster than 300 km s^{-1}.

In order to compare the models at different metallicities and with different initial masses with another quantity than the surface velocity, the ratio $v_{\mathrm{ini}}/v_{\mathrm{crit}}$ is used (see Table 1). $v_{\mathrm{crit}}^2 = GM/R_{\mathrm{eb}}(1 - \Gamma)$, where R_{eb} is the equatorial radius at break–up and Γ is the ratio of the luminosity to the Eddington luminosity. $v_{\mathrm{ini}}/v_{\mathrm{crit}}$ increases only as $r^{-1/2}$ for models with the same angular momentum (J) but lower metallicity, whereas the surface rotational velocity increases as r^{-1} ($J \sim vr$). The angular momentum could be used as well but it varies significantly for models of different initial masses. Finally, $v_{\mathrm{ini}}/v_{\mathrm{crit}}$ is a good indicator for the impact of rotation on mass loss.

In the first series of models, the aim is to scan the parameter space of rotation and metallicity with 20 $M_\odot$ models since a 20 $M_\odot$ star is not far from the average massive star concerning stellar yields. For this series, two initial rotational velocities were used at very low metallicities. The first one is the same as at solar metallicity, 300 km s^{-1}. The ratio $v_{\mathrm{ini}}/v_{\mathrm{crit}}$ decreases with metallicity (see Table 1 for the 20 $M_\odot$ models) for the initial velocity of 300 km s^{-1}. The second v_{ini} is 500 km s^{-1} at Z=10^{-5} ([Fe/H]$\sim$-3.6) and 600 km s^{-1} at Z=10^{-8} ([Fe/H]$\sim$-6.6). These values have ratios of the initial velocity to the break–up velocity, v_{ini}/v_c around 0.55, which is only slightly larger than the solar metallicity value (0.44).

The 20 $M_\odot$ model at Z=10^{-8} and with 600 km s^{-1} has a total initial angular momentum $J_{\mathrm{tot}} = 3.3\,10^{52}$ erg s which is the same as for of the solar metallicity 20 $M_\odot$ model with 300 km s^{-1} ($J_{\mathrm{tot}} = 3.6\,10^{52}$ erg s). So a velocity

of $600\,\mathrm{km\,s^{-1}}$, which at first sight seems extremely fast, is probably the average velocity at $Z=10^{-8}$.

In the second series of models, we follow the exploratory work of Meynet, Ekström & Maeder (2005) and compute models at $Z=10^{-8}$ with initial masses of 40, 60 and 85 $M_\odot$ and initial rotational velocities of 700, 800 and $800\,\mathrm{km\,s^{-1}}$ respectively. Note that, for these models as well, the initial total angular momentum is similar to the one contained in solar metallicity with rotational velocities of $300\,\mathrm{km\,s^{-1}}$. Since this is the case, velocities between 600 and $800\,\mathrm{km\,s^{-1}}$ are considered in this work as the average rotational velocities at these very low metallicities.

2.3 Simulations

The evolution of the models was followed until core Si–burning. Note that the non–rotating and fast rotating 20 $M_\odot$ models at $Z=10^{-8}$ have a strongly degenerate core such that Si–burning does not occur in the central percent of the star. It is planned to improve the model to better follow strongly degenerate core. This does nevertheless not affect the results for presented in this work. The 60 $M_\odot$ model was evolved until Ne–burning. This means that, for this model only, the yields of the heavy elements can still vary. The stellar yields are calculated as in Hirschi et al (2005). Therefore the contribution from explosive nucleosynthesis is not included and the remnant mass is determined from the CO core mass (see Maeder 1992). The impact on the results are discussed in Hirschi (2004) and we only present yields for elements which are not significantly affected by the evolution beyond our calculations. The main characteristics of the models are presented in Table 1.

2.4 20 $M_\odot$ models

2.4.1 Evolution of the internal structure

Mass loss becomes gradually unimportant as the metallicity decreases in the 20 $M_\odot$ models. At solar metallicity, the rotating 20 $M_\odot$ model loses more than half of its mass, at $Z = 0.001$, the models lose less than 15% of their mass, at $Z = 10^{-5}$ less than 3% and at $Z = 10^{-8}$ less than 0.3% (see Table 1). This means that at very low metallicities, the dominant effect of rotation is mixing for the mass range around 20 $M_\odot$. At solar metallicity and metallicities higher than about $Z = 10^{-5}$, rotational mixing increases the helium and CO core sizes (see Table 1). In particular, the oxygen yield is increased.

The impact of mixing on models at $Z = 10^{-8}$ (and at $Z = 0$ see Ekström et al 2006) is however different for an average rotation (v_{ini} =600 km s^{-1}). The impact of mixing is best pictured in the Kippenhahn diagram for this model (see Fig. 1 *right*). During hydrogen burning and the start of helium burning, mixing increases the core sizes. Mixing of helium above the core suppresses the intermediate convective zones linked to shell H–burning. So far the process is similar to higher metallicity models. However, after some

Table 1: Initial parameters of the models (columns 1–5): mass, metallicity, rotation velocity [km s^{-1}], total angular momentum [10^{53} erg s] and $v_{\mathrm{ini}}/v_{\mathrm{crit}}$. Total lifetime [Myr] and various masses [$M_\odot$] (7–10): final mass (3), masses of the helium and carbon–oxygen cores and the remnant mass.

M_{ini}	Z_{ini}	v_{ini}	$J_{\mathrm{tot}}^{\mathrm{ini}}$	$v_{\mathrm{ini}}/v_{\mathrm{crit}}$	τ_{life}	M_{final}	M_α	M_{CO}	M_{rem}
20	2e-02	300	0.36	0.44	11.0	8.7626	8.66	6.59	2.57
20	1e-03	000	–	0.00	10.0	19.5567	6.58	4.39	2.01
20	1e-03	300	0.34	0.39	11.5	17.1900	8.32	6.24	2.48
20	1e-05	000	–	0.00	9.80	19.9795	6.24	4.28	1.98
20	1e-05	300	0.27	0.34	11.1	19.9297	7.90	5.68	2.34
20	1e-05	500	0.42	0.57	11.6	19.5749	7.85	5.91	2.39
20	1e-08	000	–	0.00	8.96	19.9994	4.43	4.05	1.92
20	1e-08	300	0.18	0.28	9.98	19.9992	6.17	5.18	2.21
20	1e-08	600	0.33	0.55	10.6	19.9521	4.83	4.36	2.00
40	1e-08	700	1.15	0.55	5.77	35.7954	13.5	12.8	4.04
60	1e-08	800	2.41	0.57	4.55	48.9747	25.6	24.0	7.38
85	1e-08	800	4.15	0.53	3.86	19.8677	19.9	18.8	5.79
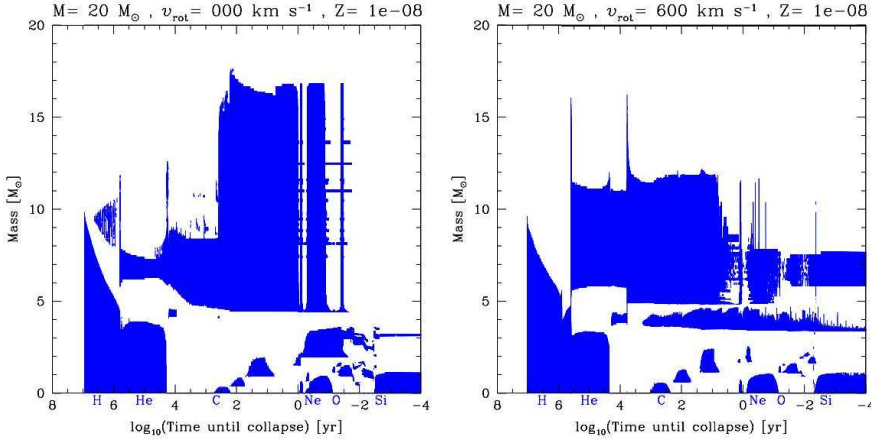
Figure 1: Kippenhahn diagrams of $20\,M_\odot$ models at $Z = 10^{-8}$ with $v_{\mathrm{ini}} = 0\,\mathrm{km\,s^{-1}}$ (*left*) and $600\,\mathrm{km\,s^{-1}}$ (*right*) (figure taken from Hirschi 2006).

Table 2: Initial mass (column 1), metallicity (2) and rotation velocity [$\mathrm{km\,s^{-1}}$] (3) and total stellar yields (wind + SN) [$M_\odot$] for carbon (4), nitrogen (5) and oxygen (6).

M_ini	Z_ini	v_ini	$^{12}\mathrm{C}$	$^{14}\mathrm{N}$	$^{16}\mathrm{O}$
20	2e-02	300	4.33e-01	4.33e-02	2.57e+00
20	1e-03	000	3.73e-01	3.31e-03	1.46e+00
20	1e-03	300	6.76e-01	3.10e-03	2.70e+00
20	1e-05	000	3.70e-01	4.27e-05	1.50e+00
20	1e-05	300	4.81e-01	1.51e-04	2.37e+00
20	1e-05	500	6.48e-01	5.31e-04	2.59e+00
20	1e-08	000	2.62e-01	8.52e-03	1.20e+00
20	1e-08	300	3.81e-01	1.20e-04	1.96e+00
20	1e-08	600	8.23e-01	5.90e-02	1.35e+00
40	1e-08	700	1.79e+00	1.87e-01	5.94e+00
60	1e-08	800	3.58e+00	4.14e-02	1.28e+01
85	1e-08	800	7.89e+00	1.75e+00	1.23e+01

time in He–burning, the mixing of primary carbon and oxygen into the H–burning shell is important enough to boost significantly the strength of the shell. As a result, the core expands and the size of the helium burning core becomes and remains smaller than in the non–rotating model (Fig. 1 *left*). The yield of $^{16}\mathrm{O}$ being closely correlated with the size of the CO core, it is therefore reduced due to the strong mixing. At the same time the carbon yield is increased. This produces an upturn of C/O at very low metallicities.

2.4.2   Stellar yields of CNO elements

The yields of $^{12}\mathrm{C}$, $^{14}\mathrm{N}$ and $^{16}\mathrm{O}$ are presented in Figs. 2 and 3 and their numerical values are given in Table 2 (see Hirschi 2006 for more details). The most stringent observational constraint at very low Z is a very high primary $^{14}\mathrm{N}$ production (Chiappini et al 2005, Prantzos 2004). This requires extremely high primary $^{14}\mathrm{N}$ production in massive stars, of the order of 0.06 $M_\odot$ per star. In Fig. 2, we can see that only the model at $Z = 10^{-8}$ and with $v_\mathrm{ini}=600\,\mathrm{km\,s^{-1}}$ can reach such high values. The bulk of $^{14}\mathrm{N}$ is produced in the convective zone created by shell hydrogen burning (see Fig. 1 *right*). If this convective zone deepens enough to engulf carbon (and oxygen) rich layers, then significant amounts of primary $^{14}\mathrm{N}$ can be produced ($\sim$0.01 $M_\odot$). This occurs in both the non–rotating model and the fast rotating model but for different reasons. In the non–rotating model, it occurs due to structure rearrangements similar to the third dredge–up at the end of carbon burning. In the model with $v_\mathrm{ini} =600\,\mathrm{km\,s^{-1}}$ it occurs during shell helium burning because of the strong mixing of carbon and oxygen into the hydrogen shell burning zone.
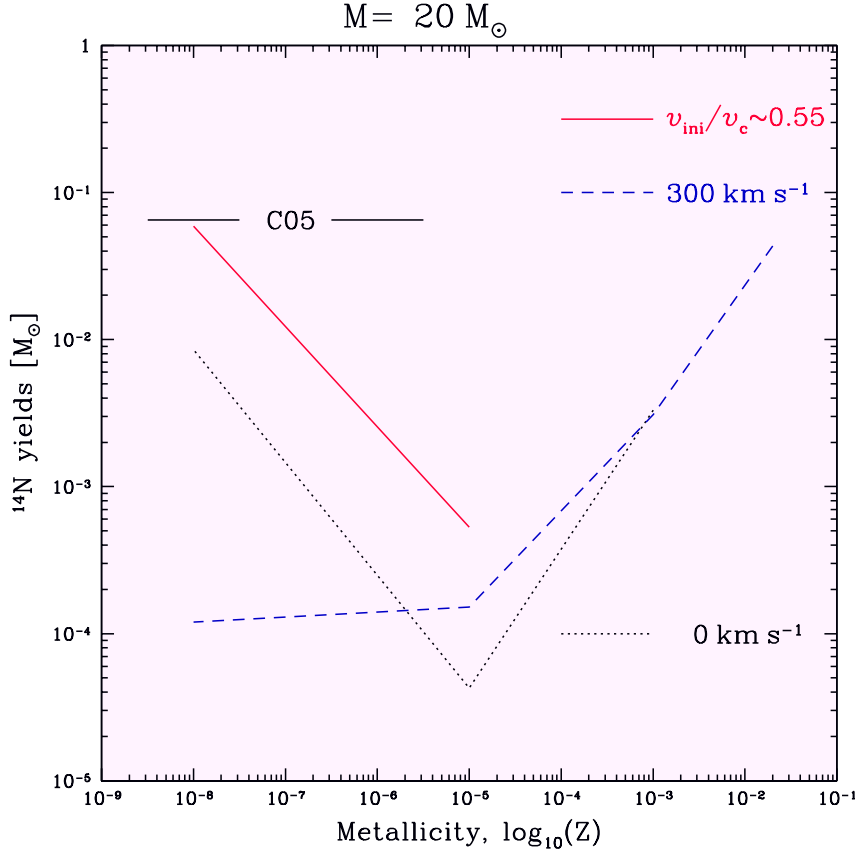
Figure 2: Stellar yields of ^{14}N as a function of the initial metallicity of the models (figure taken from Hirschi 2006). The solid red, dashed blue and dotted black lines represent respectively the models with an average rotation ($v_{ini}/v_c \sim 0.55$ and v_{ini}=500 km s^{-1} at $Z = 10^{-5}$ and v_{ini}=600 km s^{-1} at $Z = 10^{-8}$), with v_{ini}=300 km s^{-1} and without rotation. The horizontal mark with C05 in the middle corresponds to the primary ^{14}N production needed in the chemical evolution models of Chiappini et al (2005) to reproduce observations.
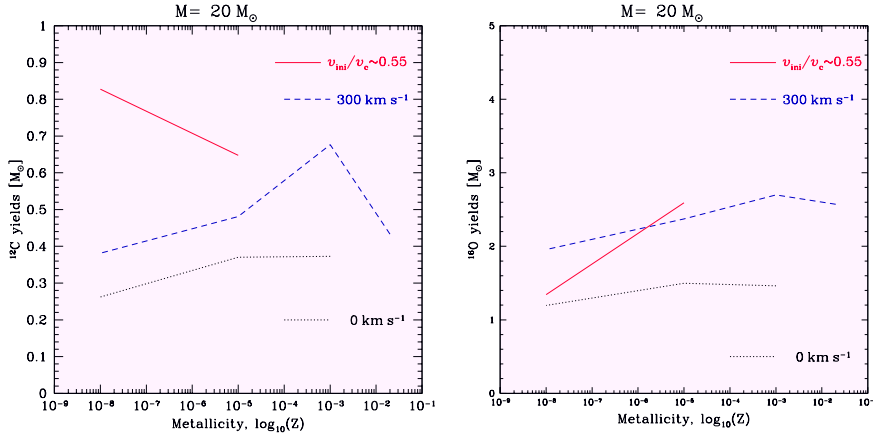
Figure 3: Stellar yields of ^{12}C (*left*) and ^{16}O (*right*) as a function of the initial metallicity of the models. The solid red, dashed blue and dotted black lines represent respectively the models with an average rotation ($v_{\mathrm{ini}}/v_c \sim 0.55$ and v_{ini}=500 km s^{-1} at $Z = 10^{-5}$ and v_{ini}=600 km s^{-1} at $Z = 10^{-8}$), with v_{ini}=300 km s^{-1} and without rotation (figures taken from Hirschi 2006).

Models with higher initial masses at $Z = 10^{-8}$ also produce large quantities of primary nitrogen. More computations are necessary to see over which metallicity range the large primary production takes place and to see whether the scatter in the yields of the models with different masses and metallicities is compatible with the observed scatter.

2.5 Models at $Z = 10^{-8}$

2.5.1 Stellar winds

Contrarily to what was initially expected from very low metallicity stars, mass loss can occur in massive stars (Meynet, Ekström & Maeder 2005). The mass loss occurs in two phases. The first phase is when the star reaches break–up velocities towards the end of the main sequence. Due to this effect stars, even metal free ones, are expected to lose about 10% of their initial masses for an average initial rotation. The fraction could be higher if the initial rotation turns out to be higher. The second phase in which large mass loss can occur is during the RSG stage. Indeed, stars more massive than about 60 $M_\odot$ at $Z = 10^{-8}$ become RSG and dredge–up CNO elements to the surface. This brings the total metallicity of the surface to values within an order of magnitude of solar and triggers large mass loss. The final masses of the models are given in Table 1. The case of the 85 $M_\odot$ model is extremely interesting (see Fig. 4 *left*) since it loses more than three quarter of its initial mass. It even becomes a WO star.
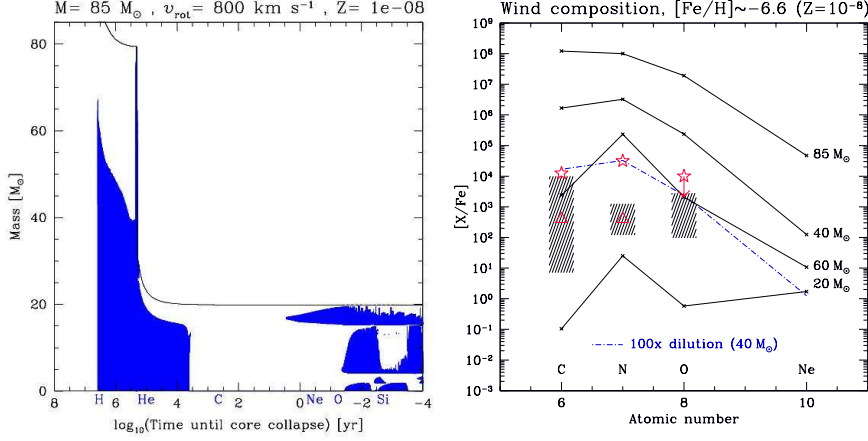
Figure 4: *Left*: Kippenhahn diagram of $85\,M_\odot$ models at $Z = 10^{-8}$ with $v_{\rm ini} = 800\,{\rm km\,s^{-1}}$. *Right*: The solid lines represent the chemical composition of the wind material of the of the different models at $Z = 10^{-8}$. The hatched areas correspond to the range of values measured at the surface of giant CEMP stars: HE 0107-5240, [Fe/H]$\simeq$ -5.3 (Christlieb 2004); CS 22949-037, [Fe/H]$\simeq$ -4.0 (Norris et al 2001, Depagne et al 2002); CS 29498-043, [Fe/H]$\simeq$ -3.5 (Aoki et al 2004). The empty triangles (Plez & Cohen 2005), [Fe/H]$\simeq -4.0$ and stars (Frebel et al 2005), [Fe/H]$\simeq -5.4$, only an upper limit is given for [O/Fe], corresponding to non-evolved CEMP stars (figures taken from Hirschi 2006).

Table 3: Initial mass (column 1), metallicity (2) and rotation velocity [km s^{-1}] (3) and stellar wind ejected masses [$M_\odot$] for carbon (4), nitrogen (5) and oxygen (6).

M_{ini}	Z_{ini}	v_{ini}	^{12}C	^{14}N	^{16}O
20	1e-08	600	3.44e-12	3.19e-10	6.69e-11
40	1e-08	700	5.34e-03	3.63e-03	2.42e-03
60	1e-08	800	1.80e-05	6.87e-04	5.49e-05
85	1e-08	800	6.34e+00	1.75e+00	3.02e+00

2.5.2 Wind composition and CRUMPS stars

In Fig. 4 (*right*), we compare the chemical composition of the wind material with abundances observed in non-evolved carbon rich extremely and ultra (Frebel et al 2005) metal poor stars. The ejected masses of the wind material are also given in Table 3. It is very interesting to see that the wind material can reproduce the observed abundance in two ways. Either, the wind material is richer than necessary and dilution (by a factor 100 for example for the 40 $M_\odot$ models and HE1327-2326) with the ISM is needed or the wind has the right enrichment (for example the 60 $M_\odot$ and HE1327-2326) and the low mass star could form from pure wind material. The advantage of the pure wind material is that it has a ratio ^{12}C/^{13}C around 5 (Meynet, Ekström & Maeder 2005) and it can explain Li depletion. With or without dilution, the wind material has the advantage that it brings the initial metallicity of the low mass star above the critical value for its formation (Bromm 2005).

3 Core collapse and explosive nucleosynthesis

3.1 Collapse, bounce, and postbounce evolution

Supernovae of type II, Ib/c are triggered by the gravitational collapse of the inner stellar core when it reaches the Chandrasekhar mass, i.e. the maximum iron core mass supported by the dominant electron pressure. Early spherically symmetric simulations (at that time adiabatic or based on local neutrino emission approximations) (Van Riper & Arnett 1978 and References therein) suggested the separation of the collapsing material into an inner and an outer core. The inner core fails only marginally to be pressure supported and the sound speed stays faster than the fluid velocity at all times. In this regime, the infall velocity increases linearly with the radius. Because the matter density and sound speed decrease with the distance from the center, there is a sonic point where the sound speed approaches the infall velocity. Outside of the sonic point, the infall velocity is larger than the sound speed and information about the collapsed core reach the outer layers only in form of a rarefaction

wave.

The essentially polytropic behavior of the equation of state allows a non-relativistic analytic investigation of collapse (Goldreich & Weber 1980, Yahil 1983) (Note that general relativistic effects decrease the mass of the inner core by $\sim 20\%$ (Liebendörfer et al. 2001, Hix et al. 2003)). The analytic investigation shows that the mass of the inner core is well approximated by

$$M_{ic} \simeq (\kappa/\kappa_0)^{3/2} M_0,$$

where M refers to the core mass and κ to the coefficient in the polytropic equation of state $p = \kappa\rho^\gamma$ with $\gamma = 4/3$. Values with index 0 belong to the marginally stable stage immediately before collapse. With the coefficient for the degenerate ultra-relativistic electron gas (Shapiro & Teukolsky 1983)

$$\kappa = \frac{\hbar c}{4} \left(3\pi^2\right)^{1/3} \left(\frac{Y_e}{m_B}\right)^{4/3},$$

one readily reproduces the conclusion that the mass of the inner core, M_{ic}, evolves proportionally to the squared electron fraction, Y_e^2. The evolution of Y_e and the entropy during collapse are determined by the interplay between three different physical processes: (i) the transition of protons to neutrons by electron capture and neutrino emission, $e^- + p \rightarrow n + \nu_e$, (ii) isoenergetic neutrino scattering off nucleons, $\nu_e + \{p, n\} \rightarrow \nu_e' + \{p, n\}$, and (iii) neutrino thermalization by neutrino scattering off electrons, $\nu_e + e^- \rightarrow \nu_e' + e^{-\prime}$. Each of these processes is rather straightforward to describe in a gas of free nucleons (Bruenn 1985). In reality, however, the by far most abundant nuclear species in the cold collapsing matter are neutron-rich heavy nuclei. While the described weak interactions basically stay the same, they rather involve nucleons bound in nuclei than free ones. This leads to the interesting expectation that the nuclear structure is probed in many nuclei that are difficult or impossible to explore under terrestrial conditions. See (Martínez-Pinedo et al. 2004) for a recent review.

(i) As the density, ρ, increases, the electron chemical potential increases with $\mu_e \propto \rho^{1/3}$ (Bethe 1990). The electrons fill higher energy levels and electron captures on free or bound protons become more frequent. As long as the density is lower than 5×10^{10} g/cm^3, the neutrinos escape freely and the deleptonization rate is determined by the electron capture rate. The electron capture rate on free protons is by two orders of magnitude larger than the one on nuclei. But the nuclei are by orders of magnitude more abundant targets. Because of a highly floating magnitude of the free proton fraction, it is difficult to decide from first principles whether electron captures on free protons or nuclei would dominate in core collapse: Due to the repulsive positive charges of the protons, nuclei are most stable in a neutron-rich configuration and the ratio of bound protons to neutrons is mainly determined by intrinsic properties of the nuclei and the entropy. Hence, small changes in the electron fraction or entropy of the fluid element cause significant changes in the small abundance of unbound free protons. A rising abundance of free protons is immediately

followed by increased electron captures, lowering the electron fraction, and thus driving back the free proton abundance. The deleptonization caused by this strong negative feedback sets an upper limit to the sustainable electron fraction in the inner core, even in the absence of other open channels for electron capture (Messer 2000, Liebendörfer et al. 2002).

However, improved electron capture rates on heavy nuclei (Langanke & Martínez-Pinedo 2002) that overcome the idealized blocking of Gamov-Teller transitions in the traditionally applied single-particle model allow the deleptonization to occur always faster than with captures on free protons alone. In fact, the most recent simulations with improved electron capture rates demonstrate that electron capture on heavy nuclei is always dominating over electron capture on free protons and that the deleptonization proceeds to significantly lower electron fractions at the center of the core than with the previous "standard" nuclear physics input, resulting in a 20% smaller inner core at bounce (Langanke et al. 2003, Hix et al. 2003, Marek et al. 2005).

(ii) The basic neutrino opacity in core collapse is provided by neutrino scattering on nucleons. Depending on the distribution of the nucleons in space and the wavelength of the neutrinos, various important coherence effects can occur: Most important during collapse is the binding of nucleons in nuclei with a density contrast of several orders of magnitude to the surrounding nucleon gas. The cross section for coherent scattering of low energy neutrinos on nuclei scales with A^2 for nuclei with atomic number A. Coherent scatterings off nuclei therefore easily dominate the scattering opacity of neutrinos on nucleons of the surrounding neutron gas (Freedman 1974). A useful comparison of inverse mean free paths at the important density $\rho = 10^{12}$ g/cm^3 is given in (Bruenn & Mezzacappa 1997). They find $\lambda_{\nu+n}/\lambda_{\nu+A} \sim 3 \times 10^{-2}$, $\lambda_{\nu+e}/\lambda_{\nu+A} \sim 2.5 \times 10^{-2}$, $\lambda_{\nu+He}/\lambda_{\nu+A} \sim 10^{-4}$, and $\lambda_{\nu+p}/\lambda_{\nu+A} \sim 5 \times 10^{-5}$.

Further corrections are necessary: with an increasing ratio between the Coulomb potential of the positively charged ions and their thermal energy, the average separation between nuclei will more strongly peak around the value of most efficient packing. The neutrino opacities are then to be corrected by an ion-ion correlation function $\langle S_{ion}(E_\nu) \rangle < 1$ (Itoh 1975, 1979, Horowitz 1997). Its consideration in core collapse simulations based on a representative nucleus lowers the trapped lepton fraction at bounce by 0.015 and increases the central entropy per baryon by $0.12k_B$ (Bruenn & Mezzacappa 1997). It is found that the sizable entropy increase is not only due to the increased deleptonization, but also to the fact that the correlation effect is most pronounced for the low energy neutrinos with long wavelengths. As current core collapse models proceed toward the inclusion of a full ensemble of nuclei, it becomes rather non-trivial how to adequately determine correlation effects in the ion mixture, see for example (Sawyer 2005) and References therein.

The situation is even more complicated in the phase transition from isolated nuclei to bulk nuclear matter where the nuclei or the holes in between them are strongly deformed. Various pasta-like shapes may be assumed. Correlation effects in this phase could also affect the neutrino opacities (Horowitz et al. 2004, Watanabe et al. 2004). For an immediate effect on core collapse,

however, it would be required that this transition phase would reach to fairly low densities in order to affect the opacities at the neutrinospheres where the neutrino luminosities and spectra are set. A detailed overview over neutrino opacities in nuclear matter has recently been given by (Burrows, Reddy & Thompson 2004). An extensive quantitative overview over most reaction rates has also been provided in the literature (Bruenn & Haxton 1991).

(iii) Neutrinos are produced by the capture of degenerate electrons from high energy levels. To some extent depending on the Q-value of the capturing nucleus, the emitted neutrino starts with a high energy of the order of the electron chemical potential. As the neutrino opacities scale with the squared neutrino energy, the initially trapped neutrinos will down-scatter to lower energies until the diffusion time scale becomes comparable to the thermalization time scale. The thermalization in current collapse models occurs through neutrino-electron scattering because the energy transfer per collision with the light electron is more efficient than with the heavier nucleons. The contribution of inelastic scattering of neutrinos off heavy nuclei depends on the individual nuclei and remains to be explored in detail.

Once nuclear densities are reached at the center of the collapsing core, repulsive nuclear forces dominate the stiffness of the equation of state. The collapse is halted by an outgoing pressure wave. Different snapshots of the velocity profile around bounce are shown in Fig. 5. The pressure wave travels through the inner core, where infall velocities are subsonic, and turns into a shock wave when it meets supersonic infall velocities at its edge. The matter in the inner core experiences a rather adiabatic pressure wave and remains at low entropy ~ 1.4 kB per baryon. The shock wave in the outer core, however, heats matter to entropies larger than ~ 6 kB per baryon so that heavy nuclei are dissociated. If the bounce-shock were to dynamically propagate through the core to expel outer layers in a prompt explosion, it would have to provide the energy to dissociate the material between the edges of the inner core and the iron core at a rate of 1.5×10^{51} erg per 0.1 M$_\odot$ of dissociated material (the shock additionally suffers from unavoidable neutrino losses).

Numerical simulations based on standard input physics and accurate neutrino transport exclude the possibility that the kinetic energy of the hydrodynamical bounce at nuclear densities drives a prompt supernova explosion (Liebendörfer et al. 2001, Bruenn et al. 2001, Rampp & Janka 2002, Thompson et al. 2003, Sumiyoshi et al. 2005). While the trajectory through core collapse determines the state of the cold nuclear matter inside the protoneutron star (PNS), the mass of the hot mantle surrounding the PNS grows by continued accretion. The infalling matter is heated and dissociated by the impact at the fairly stationary accretion front. Before about 50 ms after bounce, the entropy achieved by this shock-heating is higher than the maximum entropy obtained by infinite exposure to the prevailing neutrino field. With time ongoing, the neutrinospheres recede to smaller radii and produce a harder neutrino spectrum. On the other hand, the accretion front hydrostatically moves to larger radii where the dissipated kinetic energy of the infalling matter is smaller. Hence, only after 50 ms, when the entropy of shocked ma-
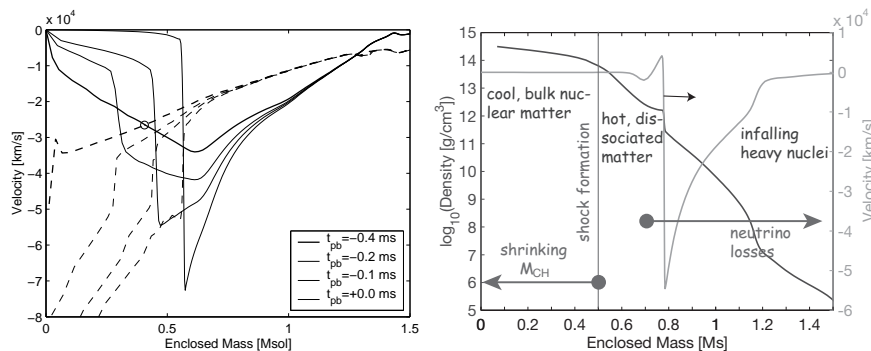
14

Figure 5: The figure on the left hand side shows velocity profiles immediately before bounce (solid lines). The maximum infall velocity at 0.4 ms before bounce marks the edge of the inner core. A circle is drawn at the sonic point, where the infall velocity is equal to the sound speed (dashed lines). The later profiles demonstrate how a pressure wave is launched at the center and runs through the inner core until it turns into a shock front close to its edge. The figure on the right hand side shows the velocity and density profiles few ms after bounce when the neutrino burst is launched. At this time the remaining shock energy (region with positive velocities) is decaying and the shock stalls into an expanding accretion front.

terial is smaller and the neutrino luminosity higher, neutrino heating becomes effective behind the shock. Behind the shock, matter continues to drift inward and to converge to higher densities. The increasing electron chemical potential blocks the electron phase space and favors antineutrino capture in the gain region below the accretion front, and electron capture in the cooling region above the PNS surface. Only expanding matter can lead to preferential neutrino capture as will be discussed in section 3.4. The gain radius separates the gain region from the cooling region. It is the radius where cooling by neutrino and antineutrino emission balances heating by neutrino and antineutrino absorption, i.e. the point where the infalling fluid element reaches equilibrium entropy in the neutrino field produced at the PNS surface. The reaction time scale in the cooling region is comparable to or faster than the infall time scale so that an infalling fluid element adheres to the equilibrium entropy on its further journey toward the surface of the NS.

One half to two thirds of the neutrino luminosity in the heating region stems from the accreting matter in the cooling region, the smaller part diffuses out of the hot PNS. Because the accretion rate reacts to neutrino heating and the neutrino luminosity to the accretion rate, the conditions at the surface of the PNS are strongly coupled to the evolution of the matter behind the accretion front. In spherical symmetry, the important neutrino transport between these layers can be numerically tackled in a fully consistent way by the accurate solution of the Boltzmann transport equation for the three

15

neutrino flavors (Rampp & Janka 2002, Thompson et al. 2003, Liebendörfer et al. 2004, Sumiyoshi et al. 2005), where the latter two references implemented all equations in general relativity. One result of these calculations was that all progenitor stars between main sequence masses of 9 and 40 $M_\odot$ showed no explosions in simulations of their postbounce evolution phases (see Fig. 9) (Liebendörfer et al. 2002). This indicates that the neutrino flux emanating from the PNS has not the ample strength to blow off the surrounding layers for a vigorous explosion without the consideration of more details. Among the reasons are the strong deleptonization during collapse, the dissociation of heavy nuclei by the shock, a slow penetration of the neutrinos from layers at high density through layers with densities between $10^{12} - 10^{13}$ g/cm^3, efficient neutrino cooling at the surface of the PNS, and fast infall velocities through the gain region (see e.g. Janka 2001).

However, spherically symmetric simulations ignore fluid instabilities that are known to exist between the protoneutron star surface and the stalled shock, as well as deep in the protoneutron star (Herant et al. 1994). There is consensus that the convective overturn in the heating region increases the heating efficiency. Heated uprising plumes free the electron phase space for neutrino absorptions and convect the energy toward the stalled shock front instead of balancing the heating in loco by neutrino emission. Additionally, cool and narrow downflows can feed the heating by continued neutrino accretion luminosity. However, first simulations in axisymmetry with energy-dependent neutrino transport do still not obtain vigorous explosions (see Buras et al. 2005 and References therein for a discussion of convection in the heating region). With respect to the convection in the PNS, the luminosities are not significantly boosted because the crucial region around the neutrinospheres appears to remain convectively stable (see Bruenn et al. 2004 and references therein for a discussion of PNS convection). As two-dimensional axisymmetric calculations are now emerging as the new standard for simulations with reliable neutrino transport, several newly appreciated phenomena are currently explored in these computationally challenging calculations (Buras et al. 2005, Walder et al. 2004, Swesty & Myra 2005, Burrows et al. 2005). The consistent coupling of the cooling and heating regions with the feedback between accretion and neutrino luminosity is much more involved in multiple dimensions than under the assumption of spherical symmetry.

3.2 Three-dimensional collapse simulations with magnetic fields

Although axisymmetric supernova models add an essential new dimension to the world of spherically symmetric models, namely the possibility to accrete and expand matter at the same time at different locations, there are still important degrees of freedom missing. Hot and cool domains in the heating and cooling regions can only assume toroidal shapes around the axis of symmetry so that convection will always imply the motion of the whole torus. Axisymmetric simulations cannot resolve small convective volumes or funnels linking

the outer layers with the surface of the PNS.

Not only the fluid instabilities may bear an inherently three-dimensional topology, also the presence of magnetic fields may introduce new degrees of freedom that can only be explored in three dimensions. First estimations of magnetic fields at the progenitor stage lead to rather low values around 10^9 Gauss (Heger et al. 2005) and stars with magnetic fields are subject to magnetic breaking of differential rotation (Maeder & Meynet 2005). The uncertainties are yet large, but nevertheless, several explosion mechanisms have been suggested based on the influence of magnetic fields: Large magnetic fields could collimate the matter outflow after the postbounce evolution and lead to jet-like explosions (LeBlanc & Wilson 1970). Smaller fields could grow by winding through differential rotation and add magnetic pressure to the fluid pressure (Akiyama et al. 2003, Ardeljan et al. 2004). In combination with differential rotation the magnetic fields could lead to the magneto-rotational instability so that the dissipation of the turbulent energy adds to neutrino heating (Thompson et al. 2004). Moreover, the magnetic field has been thought to possibly induce asymmetries to the neutrino heating (Kotake et al. 2004). Finally, it has been suggested that magnetic loops on the magnetized PNS would heat the hot mantle in analogy to the solar corona (Ramirez-Ruiz & Socrates. 2005). For all these reasons it is interesting to complement the axisymmetric simulations and accurate neutrino transport with simulations that support all degrees of freedom of three-dimensional space.

Already in one- and two-dimensional supernova models it becomes clear that the computation time spent on hydrodynamics is negligible. Most time is spent on energy-dependent neutrino transport. A systematic improvement of the neutrino transport from one to two dimensions alone required a substantial increase of computation time in yet incomplete implementations (Buras et al. 2005, Livne et al. 2004) and three-dimensional neutrino transport has not yet been attempted with a reliable resolution of the neutrino phase space. Following three-dimensional approaches of (Fryer & Warren 2002, Scheck et al. 2003), we try to balance the computation time spent on hydrodynamics and neutrino transport by maximizing the degrees of freedom in the fluid dynamics in combination with approximations in the neutrino transport. The effect of magnetic fields on the dynamics of the nucleons in the hot mantle has not yet been studied in three-dimensional numerical simulations with neutrino transport approximations. Here we continue to report on efforts in this direction (Liebendörfer, Pen & Thompson 2005).

A simple and fast three-dimensional magneto-hydrodynamics code (Pen, Arras & Wong 2003) provides the core of our simulations. It spans a central region of 600 km^3 with an equidistant resolution of 1 km in Cartesian coordinates. This covers the hot mantle and part of the infalling layers. The code has received a parallelization with MPI for cubic domain decomposition that minimizes the resources occupied on distributed memory machines by a simple and efficient reuse of buffer zones during the directional sweeps. The finite differencing is second order accurate in time and space and handles discontinuities in the conservation equations with a total variation diminishing

17

scheme. Furthermore, a specific choice of the finite differencing for the update of the magnetic field conserves its divergence to machine precision. The computational domain of the MHD code is embedded in spherically symmetrically infalling outer layers evolved by a one-dimensional hydrodynamics code.

Our collapse simulations are launched from a 15 $M_\odot$ progenitor model (Woosley & Weaver 1995). The Lattimer-Swesty equation of state (Lattimer & Swesty 1991) has been used. We imposed a rotation with angular velocity $\Omega = 31.4$ rad/s along the z-axis with a quadratic cutoff at 100 km radius. Along the same axis, we added a poloidal magnetic field of 10^{12} Gauss. The deleptonization during collapse has been parameterized in a very simple but carefully tested way (Liebendörfer 2005). An investigation of the spherically symmetric model G15 (Liebendörfer et al. 2005) with Boltzmann neutrino transport reveals that the electron fraction during infall can roughly be approximated as a function of density ρ. In our three-dimensional simulation, we update the electron fraction with $Y_e(x,y,z) = \min\left[Y_e(x,y,z), Y_e^{G15}(\rho(x,y,z))\right]$, where the function $Y_e^{G15}(\rho)$ has been read out of model G15 at the time of core-bounce. Based on this parameterized deleptonization (which also approximates the phenomenology of the various nuclear and weak interaction processes discussed in Section 3.1), the changes of the entropy and the momentum by neutrino stress are also estimated during the collapse phase. The effective gravitational potential of (Marek et al. 2005) has been used to implement general relativistic effects. Fig. 6 compares the velocity and entropy profiles in a three-dimensional collapse calculation without rotation and magnetic fields with the corresponding general relativistic spherically symmetric calculation based on Boltzmann neutrino transport. It becomes evident that the scheme reproduces the collapse phase very accurately, while important features of the postbounce phase are not yet captured, for example the neutrino burst, or neutrino heating.

Due to the rotation, the polar infall velocities are slightly larger than the equatorial infall velocities. When the central density reaches 10^{11} gcm^{-3} the magnetic field lines become visibly distorted. In the very early collapse phase this is due to matter inflow along the rotation axis, meeting at the stellar center, and pushing field lines outward into the equatorial plane. Moreover, due to the centrifugal forces, the projection of the velocities onto the plane orthogonal to the rotation axis is largest at about 100 km above and below the gravitational center. These are then the locations where the magnetic field lines condense most rapidly, bending slightly outward around the center. With ongoing collapse, this effect shifts to smaller radii and becomes more pronounced. At bounce, the magnetic field exceeds 10^{15} Gauss in these hot spots located ~ 10 km above and below the center. The field lines run along double cones aligned with the z-axis, except for the small deviation that circumvents the center. In the early shock expansion until 5 ms after bounce, the shock front is almost spherically symmetric. Afterward, the simulation becomes unrealistic, because the dynamically important neutrino burst is not implemented. Behind the expanding accretion front, entropy variations due to variations in the shock strength induce fluid instabilities that entangle the
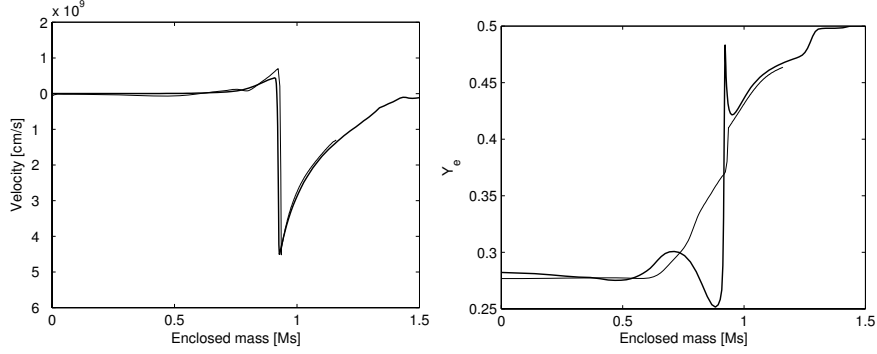
18

Figure 6: Comparison of the three-dimensional simulation with parameterized neutrino physics and effective gravitational potential (thin lines) to the corresponding general relativistic spherically symmetric simulation with Boltzmann neutrino transport (thick lines, representing model G15 in Liebendörfer et al. 2005). The figure on the left hand side shows the velocity profile at few ms after bounce. The three-dimensional model reproduces very accurately the shock position and shock strength of the model with detailed input physics. The most prominent differences are shown in the figure on the right hand side, where we compare the electron fraction. It can be seen that, as expected, the deleptonization during collapse in the inner core is well approximated. But the effects of the neutrino burst are absent in the parameterized simulation. Electron captures during the neutrino burst cause the strong Y_e-dip behind the shock and neutrino absorptions cause the Y_e-peak just ahead of the shock. See (Liebendörfer 2005) for a more detailed analysis of the parameterization.
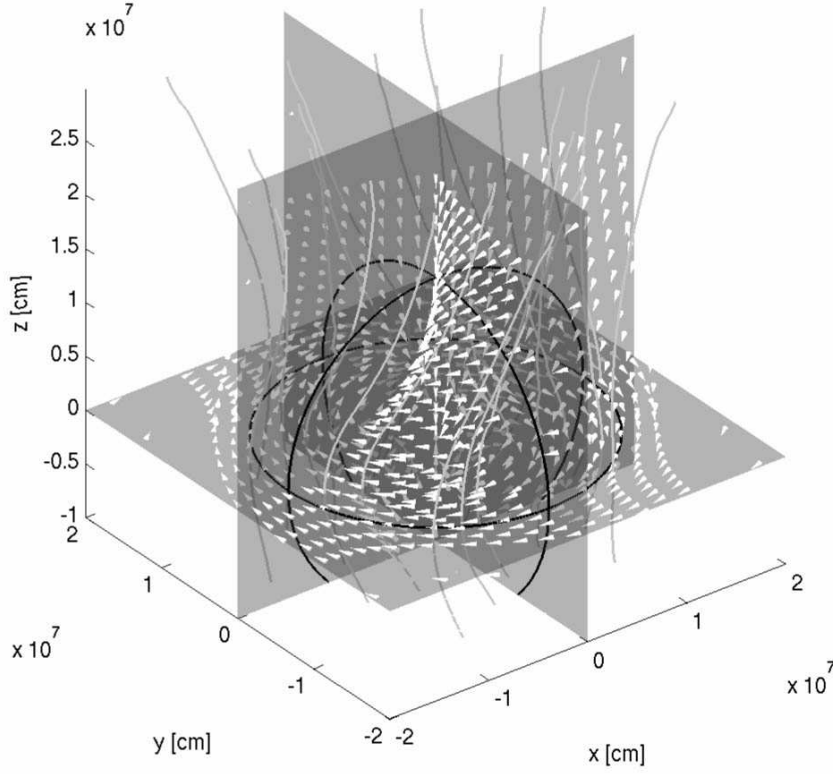
Figure 7: Snapshot of a three-dimensional simulation with rotation and magnetic fields at 150 ms before bounce. The white arrows act as mass tracers pointing out the direction of the velocities. At the beginning of the simulation all mass tracers have been placed on the three main planes. The vertical gray lines illustrate magnetic field lines that are slowly distorted by the differential rotation. The black spheres indicate the locations where the density is 10^{10} gcm^{-3}.
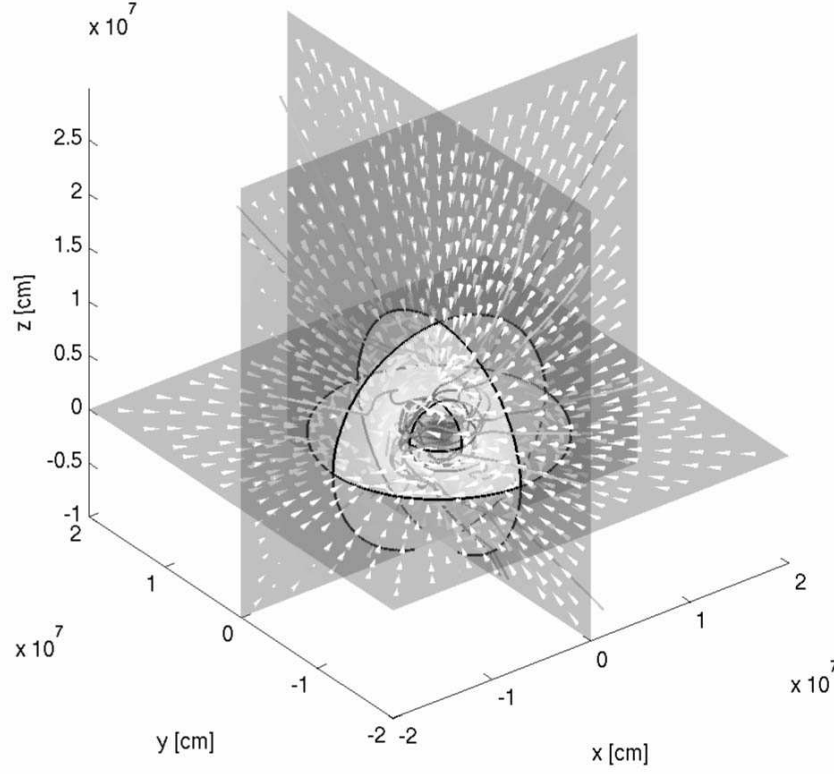
Figure 8: Snapshot of a three-dimensional simulation with rotation and magnetic fields at 5 ms after bounce. The white arrows act as mass tracers pointing out the direction of the velocities. During the simulation mass tracers are inserted at the main planes. The black spheres indicate isodensity contours at 10^{10} gcm^{-3} and 10^{12} gcm^{-3}. The latter indicates the surface of the protoneutron star at a smaller radius while the former sits in the rapidly expanding accretion front. Note that only the accretion *front* is expanding, not the hot stalled matter behind it. The shading of the main planes indicates the matter entropy ranging from ~ 1 (dark) to ~ 8 (light) Boltzmann constants per baryon. The negative entropy gradient leads to fluid instabilities that entangle the field lines in the atmosphere of the PNS. The gray lines illustrate magnetic field lines wound up by differential rotation around the surface of the protoneutron star.

magnetic field lines. Figs. 7 and 8 show a subdomain of the three-dimensional simulation at 150 ms before bounce and at 5 ms after bounce, respectively.

The simulations have been performed on 64 processors of the 528 processor McKenzie cluster at CITA. They required a wall clock time of 288 hours. If the main computational effort can be spent on magneto-hydrodynamics, three-dimensional simulations allow a spatial resolution comparable to the resolution used in spherically symmetric simulations with Boltzmann neutrino transport. Of course, this is only possible as long as the computationally expensive neutrino transport can be replaced by adequate and efficient parameterizations.

3.3 Modeling Core Collapse Supernova Nucleosynthesis

The complexity of neutrino transport and the frequent failure of self-consistent models for core collapse supernovae to produce explosions have generally divorced modeling of core collapse supernova nucleosynthesis from modeling of the central engine. Despite the (fundamental) problem that the supernova mechanism is still not understood, supernova nucleosynthesis predictions have a long tradition. All of these predictions rely on artificially introduced explosions, replacing the central engine either with a parameterized kinetic energy piston (Woosley & Weaver 1995, Rauscher et al. 2002, Chieffi & Limongi 2004) or a thermal bomb (Thielemann et al. 1996, Nakamura et al. 2001). The explosion energy and the placement of the mass cut (separating ejected matter from matter which is assumed to fall back onto the neutron star) are tuned to recover the desired (observed) explosion energy and ejected ^{56}Ni mass. Both approaches are largely compatible (Aufderheide et al. 1991) and justifiable for the outer stellar regions. It is this inner region, where most of the Fe-group nuclei are produced, which is most affected by the details of the explosion mechanism, especially the effects of the interaction of nuclei with the large neutrino flux.

The question arising is how more realistic supernova nucleosynthesis predictions could be made, given the existing problem with self-consistent explosions. Discussed improvements possibly leading to explosions are rotation and magnetic fields (Thompson 2000, Thompson et al. 2004) or uncertainties in neutrino opacities (see e.g. Burrows et al. 2004) or other microphysics properties. They would introduce additional mixing at the neutrino sphere and convective transport or change the neutrino luminosity via improved opacities. This indicates two options for successful explosions: (a) enhanced neutrino luminosities or (b) enhanced deposition efficiencies for neutrino captures in the convective layers. We use two different methods to enforce explosions in otherwise non-explosive models. In a first approach, we parameterize the neutral current neutrino scattering opacities. This helps to artificially increase the diffusive fluxes in regions of very high matter density, resulting in a faster deleptonization of the proto-neutron star such that the neutrino luminosities are boosted in the heating region. In a second approach, explosions are enforced by multiplying the reaction rates for forward and backward reactions
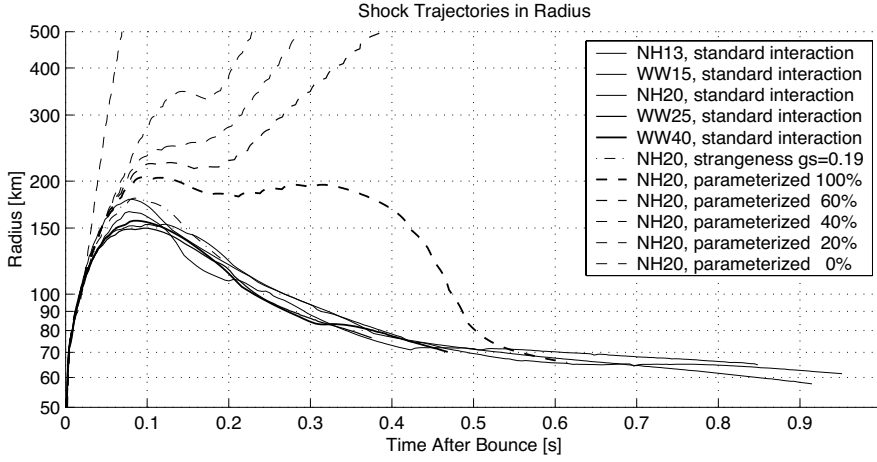
Figure 9: A sequence of collapse calculations for different progenitor masses, showing in each case the radial position of the shock front after bounce as function of time. We see that the shocks are the strongest for the least massive stars. But in these 1D calculations all of them stall, recede, and turn into accretion shocks, i.e. not causing successful supernova explosions. A reduction in the neutrino-nucleon elastic scattering, leading to higher luminosities, can help explosions to occur.

in $\nu_e + n \rightleftarrows p + e^-$ and $\bar{\nu}_e + p \rightleftarrows n + e^+$ in the heating region by equal factors. This reduces the time scale for neutrino heating as it is expected in combination with overturn in this convectively unstable domain. Both approaches allow successful explosions with a consistently emerging mass cut without the need to add external energy.

Figure 9 shows the position of the shock front as function of time for different core collapse supernova simulations. In all these models the shock front runs outwards, stalls at ~ 0.1s, and subsequently retrieves, leaving us with a non-explosive model. The dashed lines stem from models with modified neutrino-nucleon elastic scattering as described above. In the trajectories from these exploding models three phases can be distinguished: an initial outwards propagating shock, which stalls around 0.1s after bounce. But shortly before 200ms after bounce, the accretion front moves outwards again.

3.4 Nucleosynthesis Implications of Neutrino Interactions

While the importance of neutrino interactions is manifest and well documented in the ν-process and the r-process, neutrinos potentially impact all stages of supernova nucleosynthesis. Because of the impact of the neutrinos on the nucleosynthesis, the nucleosynthesis products from future explosion

23

simulations (utilizing multi-group neutrino transport) will be qualitatively different from either parametrized bomb or piston nucleosynthesis models. The dominant process are $\nu/\overline{\nu}$ and $e^{\pm}$ captures on shock dissociated free nucleons, though at later times the more poorly known $\nu/\overline{\nu}$ captures on heavy nuclei may contribute significantly.

An indispensable quantity to describe explosive nucleosynthesis in the innermost ejecta is the electron fraction Y_e (the number of electrons per nucleon). This Y_e is set by weak interactions in the explosively burning layers, i.e. electron and positron capture, beta-decays, and neutrino or anti-neutrino captures.

We examined the effects of both electron and neutrino captures in the context of recent multi-group supernova simulations. These models are based on fully general relativistic, spherically symmetric simulations (Liebendörfer et al. 2001). Pruet et al. (2005) have performed similar simulations using tracer particles from two dimensional simulations (Buras et al. 2003). In both cases, artificial adjustments to the simulations were needed to remedy the failure of the underlying models of central engines to produce explosions (see also section 3.3 for details on how to invoke an explosion in a non-explosive model). Also in both cases, the neutrino transport could not be run to later times and the simulations were mapped to a more simple model at later times. Despite these shortcomings, these simulations nevertheless reveal the significant impact of neutrino interactions on the composition of the ejecta.

We find that all our simulations that lead to an explosion by neutrino heating develop a proton-rich environment around the mass cut with $Y_e > 0.5$ (Fröhlich et al. 2006), as it is required from galactic evolution and solar abundances. Several phases can be identified in the evolution of the electron fraction of the matter that will become the innermost ejecta. At early times matter is degenerate and electron capture dominates. At the same time matter is being heated by neutrino energy deposition and subsequently, the degeneracy is lifted. While the ratio between electron captures and positron captures significantly decreases, neutrino absorption reactions start to dominate the change of Y_e. As the matter expands the density decreases and eventually the electron chemical potential drops below half the mass difference between the neutron and proton. With both neutrino absorption and emission processes favoring a higher electron fraction, Y_e rises markedly in this phase, reaching values as high as 0.55.

The global effect of this proton-rich ejecta is the replacement of previously documented overabundances of neutron rich iron peak nuclei (Woosley & Weaver 1995, Thielemann et al. 1996). Production of ^{58,62}Ni is suppressed while ^{45}Sc and ^{49}Ti are enhanced. The results (Fig. 10) for the elemental abundances of scandium, cobalt, copper, and zinc are closer to those observed (see Fröhlich et al. 2006 for details). We have found that the transformation of protons into neutrons by neutrino captures allows (n,p)-reactions to take the place of the β-decays of waiting point nuclei (with lifetimes longer than the expansion timescale), allowing significant flow to $A > 64$. We termed this process the νp-process (see Fröhlich et al. 2005 for more details) due to the
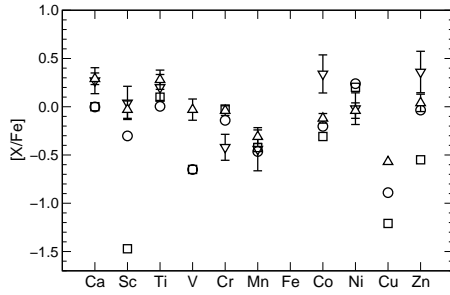
24

Figure 10: Comparison of elemental overabundances in the mass range Ca to Zn for different calculations. The triangles with error bars represent observational data. The triangles facing upwards (Gratton & Sneden 1991) originate from an analysis of stars with $-2.7 < [Fe/H] < -0.8$. The triangles facing downwards (Cayrel et al. 2004) is data for a sample of extremely metal poor stars ($-4.1 < [Fe/H] < -2.7$). The circles are abundances of our recent calculation (Fröhlich et al. 2006). The squares are abundances of Thielemann et al. 1996.

essential role of the neutrinos in producing these light p-nuclei. These results clearly illustrate the need to include the full effect of the supernova neutrino flux on the nucleosynthesis if we are to accurately calculate the nucleosynthesis from core collapse supernovae.

4   Conclusion

Two series of pre-SN models and their yields were presented in this paper. The first series consists of 20 $M_\odot$ models with varying initial metallicity (solar down to $Z = 10^{-8}$) and rotation ($v_{ini} = 0 - 600\,\mathrm{km\,s^{-1}}$). The second one consists of models with an initial metallicity of $Z = 10^{-8}$, masses between 20 and 85 $M_\odot$ and average rotation velocities at these metallicities ($v_{ini} = 600 - 800\,\mathrm{km\,s^{-1}}$). The most interesting models are the models with $Z = 10^{-8}$ ([Fe/H]~ -6.6). In the course of helium burning, carbon and oxygen are mixed into the hydrogen burning shell. This boosts the importance of the shell and causes a reduction of the size of the CO core. Later in the evolution, the hydrogen shell deepens and produces large amount of primary nitrogen. For the most massive models ($M \gtrsim 60\,M_\odot$), significant mass loss occurs during the red supergiant stage. This mass loss is due to the surface enrichment in CNO elements via rotational and convective mixing. The yields of the rotating 20 $M_\odot$ models can reproduce the observed abundances at the surface of extremely metal poor (EMP) stars and the metallicity trends. The wind of the massive models can also reproduce the CNO abundances of the carbon–rich UMPs, in particular for the most metal-poor star known to date, HE1327-2326. The inclusion of neutrino interactions in explosive nucleosynthesis changes significantly the final abundances by changing Y_e to

25

values above 0.5 in the innermost ejecta. Neutrino interactions also enables nucleosynthesis to go beyond p–rich waiting point nuclei. The new results for iron group nuclei are in much better agreement with observations of EMP stars (Sc, Ti, Ni, Zn, ...).

References

T. Abel, G. L. Bryan, and M. L. Norman, *Science* **295**, 93–98 (2002).

S. Akiyama, J. C. Wheeler, D. L. Meier and I. Lichtenstadt, *ApJ* **584** 954 (2003).

C. Angulo, M. Arnould, M. Rayet, et al, *Nuclear Physics A* **656**, 3–183 (1999).

W. Aoki, J. E. Norris, S. G. Ryan, et al, *ApJ* **608**, 971–977 (2004).

W. Aoki, A. Frebel, N. Christlieb, et al, *astro-ph/0509206* (2005).

N. V. Ardeljan, G. S. Bisnovatyi-Kogan, S. G. Moiseenko, *MNRAS* **359** 333–344 (2005).

Aufderheide, M. B., Baron, E, Thielemann, F.-K. 1991, ApJ 370, 630

T. C. Beers, G. W. Preston, and S. A. Shectman, *AJ* **103**, 1987–2034 (1992).

T. C. Beers, "Low-Metallicity and Horizontal-Branch Stars in the Halo of the Galaxy", in *ASP Conf. Ser. 165: The Third Stromlo Symposium: The Galactic Halo*, 1999, pp. 202–.

H. A. Bethe, *Rev. Mod. Phys.* **62** 801 (1990).

V. Bromm, *astro-ph/0509354* (2005).

S. W. Bruenn, *ApJS* **58** 771 (1985).

S. W. Bruenn, W. C. Haxton, *ApJ* **376** 678 (1991).

S. W. Bruenn, A. Mezzacappa, *Phys. Rev. D* **56** 7529 (1997).

S. W. Bruenn, K. R. De Nisco, A. Mezzacappa, *ApJ* **560** 326 (2001).

S. W. Bruenn, E. A. Raley, A. Mezzacappa, *astro-ph/0404099* (2004).

Buras, R., Rampp, M., Janka, H.-T., Kifonidis, K. 2003, Phys. Rev. Lett. D 90, 241101

R. Buras, M. Rampp, H.-Th. Janka, K. Kifonidis, *astro-ph/0507135*, in press (2005).

Burrows, A., Reddy, S., Thompson, T. A. 2004, Nucl. Phys. A, in press

A. Burrows, E. Livne, L. Dessart, C. Ott, J. Murphy, *astro-ph/0510687*, in press (2005).

R. Cayrel, E. Depagne, M. Spite, et al, A&A **416**, 1117–1138 (2004).

C. Chiappini, F. Matteucci, and S. K. Ballero, *A&A* **437**, 429–436 (2005).

Chieffi, A., Limongi, M. 2004, ApJ 608, 405

N. Christlieb, B. Gustafsson, A. J. Korn, et al, *ApJ* **603**, 708–728 (2004).

E. Depagne, V. Hill, M. Spite, et al, *A&A* **390**, 187–198 (2002).

P. François, F. Matteucci, R. Cayrel, et al, *A&A* **421**, 613–621 (2004).

A. Frebel, W. Aoki, N. Christlieb, et al, *Nature* **434**, 871–873 (2005).

D. Z. Freedman, *Phys. Rev. D* **9** 1389 (1974).

C. Fröhlich, P. Hauser, M. Liebendörfer, G. Martínez-Pinedo, F.-K. Thielemann, E. Bravo, N. T. Zinner, W. R. Hix, K. Langanke, A. Mezzacappa, K. Nomoto, *ApJ* **637** (2006)

C. Fröhlich, G. Martínez-Pinedo, M. Liebendörfer, F.-K. Thielemann, E. Bravo, W. R. Hix, K. Langanke, N. T. Zinner, *astro-ph/0511376* (2005)

C. F. Fryer and M. S. Warren, *ApJ* **574** 65 (2002).

I. Fukuda, *PASP* **94**, 271–284 (1982).

P. Goldreich, S. V. Weber, *ApJ* **238** 991 (1980).

Gratton, R. G., Sneden, C. 1991, A&A 241, 501

A. Heger, and S. E. Woosley, *ApJ* **567**, 532–543 (2002).

A. Heger, S. E. Woosley, H. C. Spruit, *ApJ* 626 350–363 (2005).

M. Herant, W. Benz, W. R. Hix, C. L. Fryer, S. A. Colgate, *ApJ* **435** 339 (1994).

R. Hirschi, *Ph.D. Thesis, http://quasar.physik.unibas.ch/∼hirschi/workd/thesis.pdf* (2004).

R. Hirschi, G. Meynet, and A. Maeder, *A&A* **425**, 649–670 (2004).

R. Hirschi, G. Meynet, and A. Maeder, *A&A* **433**, 1013–1022 (2005).

R. Hirschi, *A&A, in prep* (2006).

W. R. Hix, et al., *Phys. Rev. Lett.* **91** 201102 (2003).

C. J. Horowitz, *Phys. Rev. D* **55** 4577 (1997).

C. J. Horowitz, M. A. Pérez-García, J. Piekarewicz, *Phys. Rev. C* **69** 045804 (2004).

C. A. Iglesias, and F. J. Rogers, *ApJ* **464**, 943– (1996).

G. Israelian, A. Ecuvillon, R. Rebolo, R. García-López, P. Bonifacio, and P. Molaro, *A&A* **421**, 649–658 (2004).

N. Itoh, *Progress of Theoretical Physics* **54** 1580 (1975).

N. Itoh, H. Totsuji, S. Ichimaru, H. E. Dewitt, *ApJ* **234** 1079 (1979).

Y. I. Izotov, and T. X. Thuan, *ApJ* **602**, 200–230 (2004).

H.-Th. Janka, *A&A* **368**, 527–560 (2001).

K. Kotake, S. Yamada, K. Sato, *ApJ* **618** 474–484 (2004).

K. Langanke, G. Martínez-Pinedo, *Rev. Mod. Phys.* **75** 819 (2003).

K. Langanke, *et al.*, *Phys. Rev. Lett.* **90** 241102 (2003).

J. Lattimer and F. D. Swesty, *Nucl. Phys. A* **535** 331 (1991).

J. M. LeBlanc, J. R. Wilson, *ApJ* **161** 541 (1970).

Liebendörfer, M., Mezzacappa, A., Thielemann, F.-K., Messer, O. E. B., Hix, W. R., Bruenn, S. W. 2001, Phys. Rev. D 63, 103004

M. Liebendörfer, O. E. B. Messer, A. Mezzacappa, R. W. Hix, F.-K. Thielemann, K. Langanke, in *Proceedings of the 11th Workshop on "Nuclear Astrophysics"*, edited by W. Hillebrandt, E. Müller (Ringberg Castle, Tegernsee, Germany, 2002), pp. 126–131.

M. Liebendörfer, O. E. B. Messer, A. Mezzacappa, S. W. Bruenn, C. Y. Cardall, F.-K. Thielemann, *ApJS* **150** 263–316 (2004).

M. Liebendörfer, M. Rampp, H.-Th. Janka, A. Mezzacappa, *ApJ* **620** 840–860 (2005).

M. Liebendörfer, U. Pen and C. Thompson, *Nuclear Physics A* **758** 59–62 (2005).

M. Liebendörfer, *ApJ* **633** 1042–1051 (2005).

E. Livne, A. Burrows, R. Walder, I. Lichtenstadt and T. A. Thompson, *ApJ* **609** 277 (2004).

A. Maeder, *A&A* **264**, 105–120 (1992).

A. Maeder, E. K. Grebel, and J.-C. Mermilliod, *A&A* **346**, 459–464 (1999).

A. Maeder, G. Meynet, *A&A* **440** 1041–1049 (2005).

A. Marek, H.-Th. Janka, R. Buras, M. Liebendörfer, M. Rampp, *A&A* **443** (2005).

A. Marek, H. Dimmelmeier, H.-Th. Janka, E. Mueller, R. Buras, *astro-ph/0502161*, in press (2005).

G. Martínez-Pinedo, M. Liebendörfer, and D. Frekers, *astro-ph/0412091* (2004).

O. E. B. Messer, Ph.D. thesis, University of Tennessee (2000).

G. Meynet, S. Ekström, and A. Maeder, *A&A accepted* (2005).

Nakamura, T., Umeda, H., Iwamoto, K., Nomoto, K., Hashimoto, M., Hix, W. R., Thielemann, F.-K. 2001, ApJ 555, 880

J. E. Norris, S. G. Ryan, and T. C. Beers, *ApJ* **561**, 1034–1059 (2001).

U. Pen, P. Arras and S. Wong, *ApJS* **149** 447 (2003).

B. Plez, and J. G. Cohen, *A&A* **434**, 1117–1124 (2005).

N. Prantzos, *astro-ph/0411392, NIC8* (2004).

Pruet, J., Woosley, S. E., Buras, R., Janka, H.-T., Hoffman, R. D. 2005, ApJ 623, 325

M. Rampp, H.-T. Janka, *Astron. & Astrophys.* **396** 361 (2002).

E. Ramirez-Ruiz and A. Socrates, *astro-ph/0504257* (2005).

Rauscher, T., Heger, A., Hoffman, R. D., Woosley, S. E. 2002, ApJ 576, 323

S. G. Ryan, W. Aoki, J. E. Norris, and T. C. Beers, *astro-ph/0508475, ApJ, in press* (2005).

R. F. Sawyer, *Phys.Lett. B* **630** 1–6 (2005).

L. Scheck, T. Plewa, H.-T. Janka, K. Kifonidis, E. Mueller, *Phys.Rev.Lett.* **92** 011103 (2004).

S. L. Shapiro, S. A. Teukolsky, *Black Holes White Dwarfs and Neutron Stars: The Physics of Compact Objects* (Wiley-Interscience, New York, 1983).

M. Spite, R. Cayrel, B. Plez, et al, *A&A* **430**, 655–668 (2005).

K. Sumiyoshi, S. Yamada, H. Suzuki, H. Shen, S. Chiba, H. Toki, *ApJ* **629** 922–932 (2005).

F. D. Swesty and E S. Myra, *J.Phys.Conf.Ser.* **16** 380–389 (2005).

Thielemann, F.-K., Nomoto, K., Hashimoto, M. 1996, ApJ 460, 408

Thompson, C. 2000, ApJ 534, 915

T. A. Thompson, A. Burrows, P. A. Pinto, *ApJ* **592** 434 (2003).

Thompson, T. A., Quataert, E., Burrows, A., *ApJ* **620** 861–877 (2005).

H. Umeda, and K. Nomoto, *ApJ* **565**, 385–404 (2002).

H. Umeda, and K. Nomoto, *Nature* **422**, 871–873 (2003).

K. A. van Riper, W. D. Arnett, *ApJS* **225**, L129 (1978).

J. S. Vink, and A. de Koter, *astro-ph/0507352* (2005).

R. Walder, A. Burrows, C.D. Ott, E. Livne, I. Lichtenstadt, M. Jarrah, *ApJ* **626** 317–332 (2005).

G. Watanabe, K. Sato, K. Yasuoka, T. Ebisuzaki, *Phys. Rev. C* **69** 055805 (2004).

S. E. Woosley, T. A. Weaver, *ApJS* **101** 181 (1995).

A. Yahil, *ApJ* **265** 1047 (1983).